

Structure, Wrinkling, and Reversibility of Langmuir Monolayers of Gold Nanoparticles

David G. Schultz,[†] Xiao-Min Lin,[‡] Dongxu Li,[§] Jeff Gebhardt,[†] Mati Meron,[†]
P. James Viccaro,[†] and Binhua Lin^{*,†}

The Center for Advanced Radiation Sources, The University of Chicago, Chicago, Illinois 60637, Materials Science Division, Chemistry Division and Center for Nanoscale Materials, Argonne National Laboratory, Argonne, Illinois 60439, and Chemistry Department, The University of Chicago, Chicago, Illinois 60637

Received: June 19, 2006; In Final Form: September 27, 2006

The assembly of nanoparticles into large, two-dimensional structures provides a route for the exploration of collective phenomena among mesoscopic building blocks. We characterize the structure of Langmuir monolayers of dodecanethiol-ligated gold nanoparticles with *in situ* optical microscopy and X-ray scattering. The interparticle spacing increases with thiol concentration and does not depend on surface pressure. The correlation lengths of the Langmuir monolayer crystalline domains are on the order of five to six particle diameters. Further compression of the monolayers causes wrinkling; however, we find that wrinkled monolayers with excess thiol can relax to an unwrinkled state following a reduction of surface pressure. A theoretical model based on van der Waals attraction and tunable steric repulsion is adopted to explain this reversibility.

I. Introduction

Nanoparticles exhibit a wealth of size-dependent optical, electronic, and chemical properties when their sizes are comparable to or smaller than certain intrinsic physical length scales.^{1–4} One of the goals of nanotechnology is to incorporate such particles within larger structural hierarchies in which interparticle coupling effects could result in new collective phenomena.^{5–7} Of particular interest is the controllable organization of nanoparticles into two-dimensional (2D) superlattices, in which collective optical response,⁸ electron tunneling behavior,^{9–11} and chemical sensing¹² can be explored and directly compared to theoretical predictions.^{13,14}

Among the various techniques used to create 2D assembly of colloidal nanoparticles, the droplet evaporation^{15–19} and Langmuir–Blodgett (LB) techniques^{20–23} are most widely used. The process of evaporation-induced self-assembly is complicated by complex phenomena such as solvent convection¹⁶ and solvent dewetting on the substrate.¹⁷ As a result, the final products are typically mixtures of two- and three-dimensional superlattices,¹⁸ 2D films containing fractal-like aggregates, or highly percolated 2D networks.^{16,17,19} Highly ordered 2D superlattices of gold nanoparticles with domain sizes of tens of micrometers were recently shown to form at the liquid–air interface during droplet evaporation.²⁴ *In situ* small-angle X-ray scattering²⁵ and optical microscopy²⁶ revealed that 2D superlattice formation is affected by solvent evaporation kinetics as well as by particle–interface interactions. Furthermore, the interaction of the particle with the interface was found to be highly dependent upon the concentration of excess dodecanethiol molecules.

In comparison, the self-organization of colloidal nanoparticles via the LB technique has proven to be a straightforward and highly reproducible method for the production of uniform 2D structures for a variety of different types of nanoparticles.^{20–23,27–29}

Monolayers of noble metal nanoparticles created by the LB technique have been especially popular objects of study, in part because the synthesis of such particles has been well established in the past decade.^{30,31} Furthermore, the ability to form stable 2D structures of noble metal particles is largely due to the fact that the interparticle van der Waals attraction is on the order of thermal energy at room temperature when the particle separation is near 1–2 nm.^{32,33} This separation may be conveniently maintained through the use of appropriate surface ligands. Also contributing to this interest is the fact that the large linear and nonlinear dielectric susceptibilities of noble metal nanoparticles have been observed to contribute to the unique optical and electric properties of nanoparticle monolayers prepared by the LB technique.³⁴ For example, the metal-to-insulator transition as a function of interparticle separation was documented for monolayers containing silver nanoparticles.³⁵ Films containing noble metal colloidal particles could also be used as electrical, mechanical, and biosensing devices.^{36–39}

Even though the LB technique is widely used, the structural evolution of 2D colloidal arrays on liquid surfaces as a function of increasing surface pressure is not well understood. In this work, we use *in situ* optical microscopy and X-ray scattering to study the monolayer formation process of gold nanoparticles on the surface of water. The combination of these two techniques provides information on both micro- and mesoscopic-length scales. Optical microscopy offers valuable qualitative information about macroscopic phases and phase transitions. X-ray scattering provides information about packing symmetry and interparticle spacing within the plane of the monolayer and also about particle organization in the direction normal to this plane.⁴⁰ We found that the interparticle spacing within the monolayer is primarily determined by the concentration of dodecanethiol in the colloid solution and does not depend on surface pressure. For nanoparticles that are well passivated with dodecanethiol molecules, the average interparticle gap is about 1.5 times the dodecanethiol chain length. However, for nanoparticles that have been repeatedly washed and that are deficient of surface thiol molecules, the average interparticle gap is smaller than the thiol

* Corresponding author. E-mail: lin@cars.uchicago.edu.

[†] The Center for Advanced Radiation Sources.

[‡] Materials Science Division, Chemistry Division and Center for Nanoscale Materials.

[§] Chemistry Department, The University of Chicago.

chain length. We found that wrinkles consisting of multilayers of nanoparticles start to develop when the surface pressure exceeds certain limits for both types of colloids. The reversibility of these multilayer wrinkles depends on the concentration of thiol. We discuss the mechanism of this reversibility in terms of a theoretical model developed previously.³³

II. Experimental Section

A. Nanoparticle Synthesis. A highly monodisperse ($\Delta D/D \sim 8\%$) colloid of dodecanethiol-ligated gold nanoparticles suspended in heptane is used in the present study. The average diameter of 6 nm for these particles is determined from transmission electron microscopy (TEM) and is verified by our X-ray scattering data. Nanoparticles are synthesized in toluene with didodecyldimethylammonium bromide (DDAB) as the initial surfactant. Dodecanethiol is used to replace the DDAB on the nanoparticle surface through a ligand-exchange reaction. The particle size distribution is narrowed by a digestive ripening process developed earlier.⁴¹ Excess thiol molecules are removed by repeatedly precipitating and washing with ethanol until the S–H stretching mode is no longer detected in the infrared spectroscopy measurement. The well-washed nanoparticles are then dissolved in heptane at a concentration of 1.5×10^{14} particles/mL, as estimated from the surface pressure–area isotherm of the nanoparticle monolayers on the surface of water. Two types of monolayers are prepared for these measurements. In the first, the well-washed nanoparticle solution is spread directly on the surface of water. In the second, an additional amount of dodecanethiol is added to the solution prior to spreading. This excess amount follows the ratio of 6 μ L of thiol to 1 mL of nanoparticle solution. Hereafter these monolayers are referred to simply as “Au” and “T-Au”, respectively.

B. Langmuir Trough. Monolayers are prepared in a custom-built Langmuir trough, designed to accommodate both optical and X-ray measurements. It is equipped with a Teflon block barrier and Wilhelmy plate tensiometer, both of which are controlled by an interface unit (Nima Technology). The trough is enclosed in a hermetically sealed box. This feature allows us to purge the interior with helium and to thereby reduce the absorption of X-rays by air. Pure water (Millipore) is used as the subphase for all monolayers, and its temperature is maintained at 33 ± 0.2 °C for all measurements. A compression rate of 1 cm²/s is used in all surface pressure–area isotherms. Microscope images are obtained with a home-built device consisting of a 50 \times objective (Mitutoyo) mounted via an 40 mm extension tube onto a high-sensitivity CCD camera (Cohu). Motorized stages permit focusing and lateral translation of the microscope.

C. X-ray Measurements. Experiments are conducted at the ChemMatCARS synchrotron facility at the Advanced Photon Source. The liquid surface instrument we use for X-ray measurements is described in detail elsewhere.⁴² Figure 1 shows the geometry we employ. All measurements are conducted using a photon wavelength of 1.24 Å. Specularly reflected signal is collected as a function of scattering angle, using a NaI scintillation detector (Oxford Instruments). In-plane diffraction data are collected using a one-dimensional wire detector (Molecular Metrology) oriented along the surface normal and scanned in the horizontal direction. The angular acceptance of this detector ($\pm 0.08^\circ$) is determined by Soller slits. All X-ray measurements described in this paper are made within 12 h of monolayer creation. Separate monolayers are prepared for optical microscopy using the same sample.

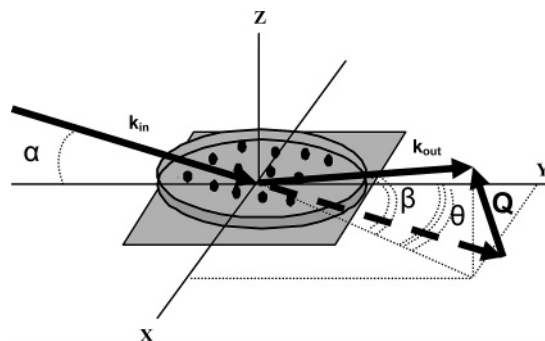


Figure 1. X-ray scattering geometry used in our experiment. The monolayer sample is sitting in the X-Y plane. The incident and scattered X-rays are along the direction of k_{in} and k_{out} , respectively. The scattering wavevector is indicated by vector Q .

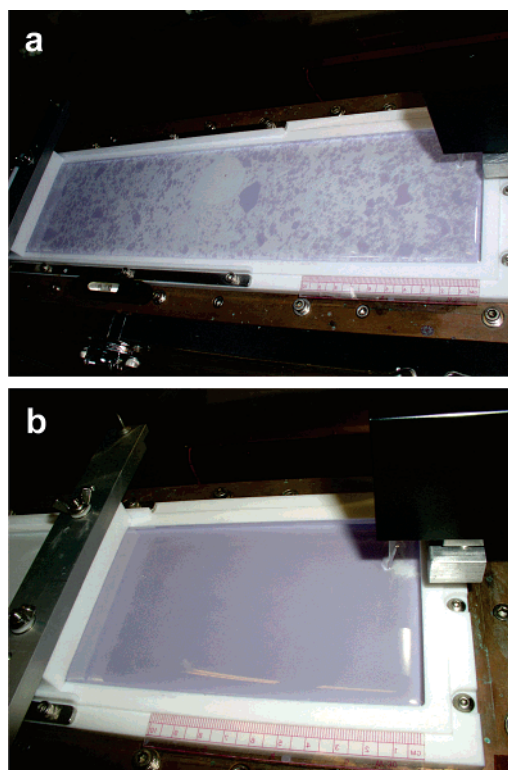


Figure 2. (a) T-Au monolayer immediately after spreading. Barrier is at left and pressure sensor is at right. (b) Appearance of a typical gold nanoparticle monolayer. The monolayer is characterized by its uniform blue color.

III. Results and Discussion

A. Surface Pressure–Area Isotherms. Immediately after colloid deposition, small islands with dimensions up to 1 cm spontaneously form on the surface of the water (Figure 2a). Their coloration, due to coupled surface plasmon resonance, makes it very easy to gauge surface coverage visually. Island formation in gold nanoparticle colloids spread at the air–water interface has been observed by others and was found to depend on nanoparticle concentration and solvent type.^{43,44} Huang et al. suggested that island formation is driven by surface tension effects of the evaporating solvent.⁴³ They found that a high concentration (0.6 mg/mL) of nanoparticles correlated with the formation of permanent voids (~ 10 nm) in the resulting LB monolayer, which could only be eliminated by compressing the monolayer to high pressures (> 20 mN/m). By comparison, the concentration we use is lower (~ 0.3 mg/mL), and we found that the use of even lower concentrations yields no difference

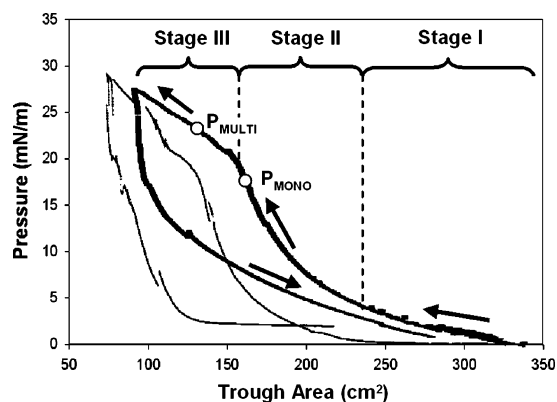


Figure 3. Surface pressure–area isotherms for Au (thin) and T-Au (bold) monolayers. For clarity, only the T-Au isotherm is labeled. Brackets indicate compression stages. Solid arrows indicate the sequence of compression followed by expansion. Hollow circles indicate the locations along the T-Au isotherm where X-ray measurements were taken.

in the final structure of the monolayer. X-ray evidence discussed in the next section supports the idea that these macroscopic islands consist of many randomly oriented, crystalline domains.

Similar to a previous study,⁴⁴ we can divide the compression of the Au and T-Au monolayer into three different stages based on the overall structural change of the monolayer identified by visual observation under the microscope, which is also reflected in the change of average isotherm curvature. Figure 3 shows a comparison of the isotherms recorded at 33 °C. Compression stages (indicated with single brackets) and the points along the isotherm at which X-ray measurements are conducted (indicated with hollow circles) are shown for the T-Au monolayer only. The Au isotherm is not labeled, but it has a similar shape (albeit shifted to lower area per particle). The small kinks and various sharp drops in the isotherms are caused by temporarily stopping the compression in order to carry out measurements. The decrease of surface pressure during these pauses accompanies the relaxation of structures within the forming monolayer. However, the surface pressure recovers quickly and increases along the same slope once the compression resumes, indicating that the surface pressure is mainly determined by the degree of jamming between domains. When the barrier motion is temporarily halted, local interdomain relaxation releases the pressure built up during compression.

Stage I compression gathers the macroscopic islands together like rigid “puzzle pieces”. These islands rotate and break apart to accommodate each other until the visible gaps are reduced to less than 1 mm. In the case of the T-Au monolayer, this is accompanied by a gradual rise in pressure. In the case of Au, the overall pressure increase in stage I is quite small and terminates at a “knee” of around 160 cm². This difference may be explained by the fact that unevaporated dodecanethiol molecules in the forming T-Au monolayer collect within the interstices of the many crystalline domains of gold particles formed after evaporation of the spreading solvent. These molecules increase the range of steric repulsion between the domains.

At the beginning of stage II compression, both monolayers appear uniform and completely covered to the naked eye (Figure 2b). However, microscopic views reveal the existence of many small voids in the monolayer, which disappear completely at the end of this stage. In the case of T-Au, microscopic liquid droplets (Figure 4a) become visible at the completion of stage II compression. These droplets most likely consist of excess unbound dodecanethiol molecules, since the heptane evaporates

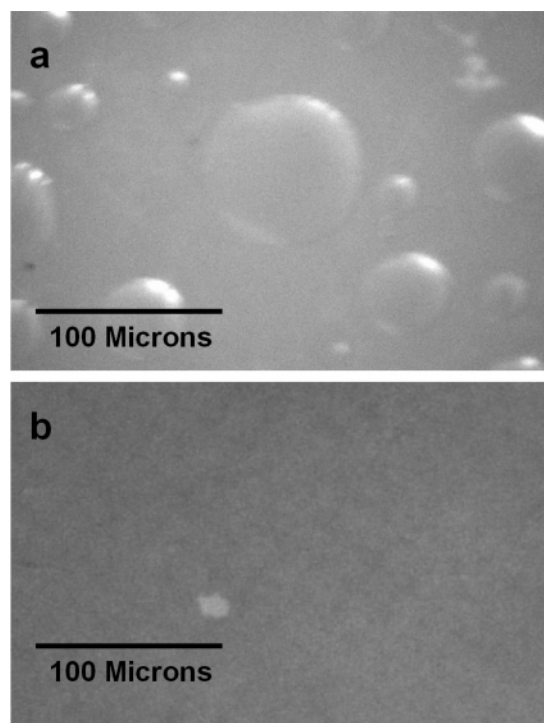


Figure 4. Optical microscope images of T-Au monolayer showing: (a) excess liquid droplets in the monolayer immediately after compression to P_{MONO} , and (b) the same region after a 1 h wait. A small void in the monolayer is visible slightly lower left of center.

much more rapidly. In the sealed trough enclosure they evaporate over the course of 1 h, and the surface becomes largely featureless and is characterized by a single shade (Figure 4b). X-ray measurements (discussed in the next section) indicate that full-coverage T-Au and Au monolayers are formed at the end of stage II compression. This point is labeled “ P_{MONO} ” on the T-Au isotherm. Compression beyond P_{MONO} results in a change in the isotherm’s slope. Comparison of the isotherms of the two types of monolayer clearly shows that compared to Au the stage II portion for T-Au is shifted to larger areas per particle. This is due to the added steric repulsion of excess dodecanethiol. The effect of the excess thiol on interparticle spacing is the subject of the latter part of this paper.

Further compression causes both monolayers to wrinkle, and this transition occurs at the same pressure in both types of monolayer. Wrinkling occurs in conjunction with a rollover in the slope of each isotherm, marking the transition from stage II to stage III. Wrinkles first appear as dark lines, a few micrometers thick, and generally run parallel to the edge of the inward-moving barrier. These lines grow in width and length until they become many centimeters long and are easily visible to the eye. For the Au monolayer, wrinkles develop almost entirely within a few centimeters of the advancing barrier. In the case of T-Au, the wrinkles form more uniformly throughout the length of the film, though a larger number still form near the barrier. X-ray measurements on multilayer structures are recorded at “ P_{MULTI} ”, at which point wrinkles are clearly visible within regions sampled by X-rays.

B. X-ray Measurements. X-ray reflectivity measurements probe the monolayer structure in the direction normal to the air–water interface and are analyzed to provide an electron density profile along this coordinate.⁴⁵ Figure 5a shows reflectivity data taken from a completely formed T-Au monolayer recorded at P_{MONO} . Overlaid on the data are the best-fit results generated using an in-house developed algorithm (see

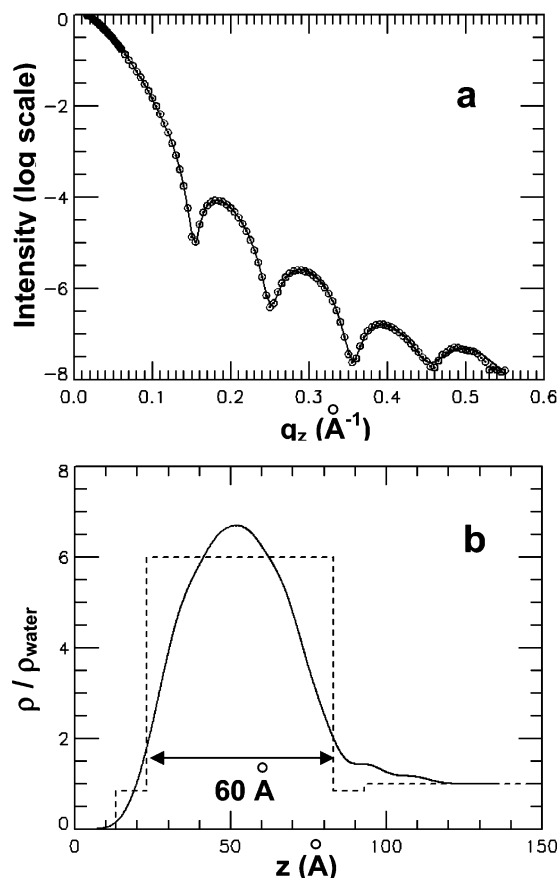


Figure 5. (a) Reflectivity from T-Au monolayer (circles) and best fit (solid line). (b) Fitted electron density profile in real space (solid line). Dashed box cartoon illustrates the relationship between the profile and the known particle diameter.

Supporting Information) based on a scheme proposed earlier by Parratt.⁴⁶ Part b of Figure 5 shows the real-space electron density profile generated by the fit. The profile shows the variation in density along the z -axis (normal to the interface) as one goes from air ($\rho = 0$), through the monolayer ($\rho \sim 6$), and into water ($\rho = 1$). The peak electron density ($\rho \sim 6$) is about half of the calculated density for crystalline gold ($\rho \sim 13$), in agreement with what one would expect if the net quantity of gold contained in the nanoparticles was distributed uniformly ("smeared") within the plane of the monolayer (assuming lattice symmetry and spacing determined by the X-ray diffraction measurements described later). A box cartoon illustrates the relationship of the fit profile to known particle diameter. The reflectivity data, its fit, and the corresponding electron density profile for the Au monolayer are essentially identical to the data shown in part a of Figure 5 and therefore are not shown.

By comparison, part a of Figure 6 shows the reflectivity obtained from a *wrinkled* T-Au monolayer, recorded at P_{MULTI} . The fit to these data yields a trilayer of nanoparticles in real space (part b of Figure 6), and a simplistic box cartoon is again overlaid on the electron density profile to illustrate the relationship between peak spacing and particle diameter. We obtain very similar data for the wrinkled Au monolayer, which can be fitted with a trilayer model as well. Fits yielding two- and four-layer structures, while reproducing many key features in the reflectivity data, nonetheless do not agree as well as the trilayer fit. We infer from the trilayer result that the monolayer buckles and then folds over like a piece of paper. Although we cannot directly observe such buckling events, the trilayer structure suggested by the reflectivity data can be most simply explained by the type of folding described above.

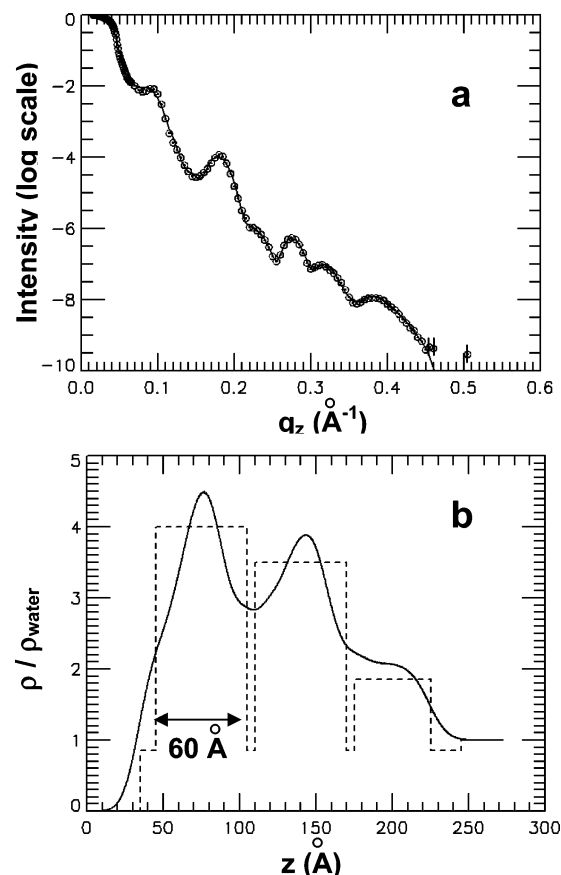


Figure 6. (a) Reflectivity from wrinkled T-Au monolayer (circles) and best fit (solid line). (b) Fitted electron density profile in real space (solid line). Dashed box cartoon illustrates the relationship between the profile and the known particle diameter.

Grazing incidence X-ray diffraction (GIXD) measurements provide information about nanoparticle packing symmetry and spacing within the plane of the air–water interface. GIXD is the result of momentum transfer to the 2D reciprocal lattice at the interface. The GIXD pattern measured for the Au monolayer at P_{MONO} is shown in Figure 7a. Diffraction peaks are evident along the q_{xy} direction (sample horizon). The strong specular reflection near $q_{xy} = 0$ \AA^{-1} is not shown, since it would obscure the other features. The pattern in Figure 7a also reveals the effect of form factor scattering. This is essentially small-angle scattering that depends on particle size and shape. For example, the strong, first-order peak near 0.1 \AA^{-1} is modulated in the q_z direction by form factor scattering from the gold particle cores. The superimposed rings in Figure 7a represent the oscillatory minima predicted for form factor scattering from 60 \AA solid spheres. These rings were fit to the GIXD pattern by eye with an estimated uncertainty of ± 0.5 \AA . We assume that the thiol shell contributes negligibly to the scattering diameter, since its density is close to that of the surrounding water.

Comparison of GIXD from the Au and T-Au monolayers indicates that interparticle spacing depends on thiol concentration. Figure 7b shows the integrated GIXD data for the Au and T-Au monolayers as a function of q_{xy} , using an integration range of $0 < q_z < 0.1$ \AA^{-1} . We assign the Miller indices at the bottom of the figure to the GIXD peaks measured for the Au monolayer. The calculated positions and intensities are indicated by the vertical bars. The calculation assumes a hexagonal lattice and uses the lattice spacing as the fit parameter. We determine the center-to-center spacing of the particles in each monolayer by performing a least-squares fit to the first four diffraction peaks as a function of their Miller indices. The uncertainty in the center

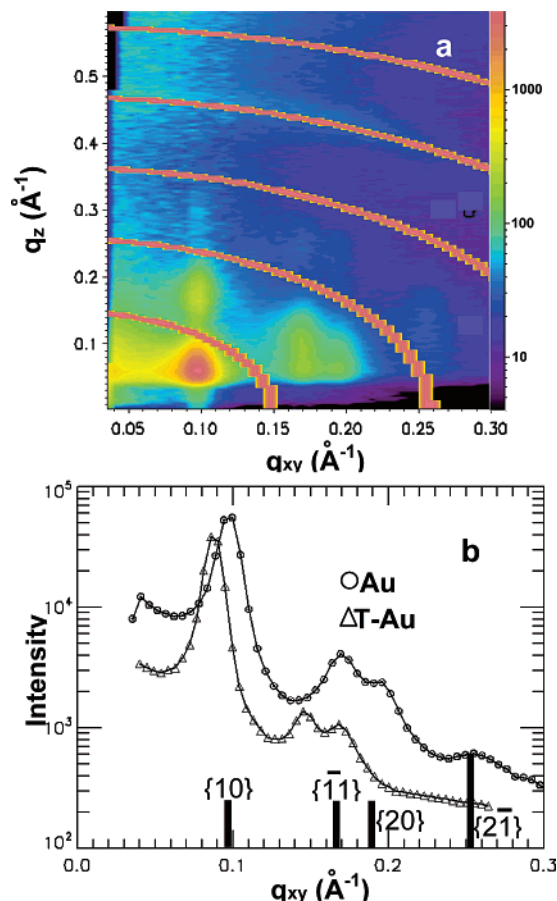


Figure 7. (a) GIXD from Au monolayer. Superimposed rings show the locations of minima in form factor scattering for solid spheres of diameter 60 Å. Scale to the right indicates intensity. (b) Comparison of GIXD, integrated along the q_z direction, for Au (circles) and T-Au (triangles), shows shift of peaks to lower q_{xy} after the addition of excess thiol. The calculated locations and relative intensities for diffraction from the Au monolayer are indicated along the ordinate. They are labeled with the corresponding Miller indices.

position determined for each peak used in the fit is $\pm 0.0025 \text{ Å}^{-1}$. Peak analysis results in center-to-center values of $74 \pm 0.8 \text{ Å}$ (Au) and $85 \pm 2 \text{ Å}$ (T-Au). These values correspond to footprints of roughly $4800 \text{ Å}^2/\text{particle}$ (Au) and $6250 \text{ Å}^2/\text{particle}$ (T-Au), with an estimated error of $\pm 5\%$. The lower number density of particles in the T-Au monolayer (roughly three-fourths that of Au) accounts for the difference in normalized intensities between the monolayers, evident in Figure 7b.

Interparticle spacing does not vary as the pressure is increased from nearly zero to P_{MONO} . Figure 8 shows the first three diffraction peaks of a partially thiolated T-Au film⁴⁷ recorded at two surface pressures. The top profile corresponds to a pressure near zero, and the bottom is obtained at P_{MONO} . No shift in peak position is evident in this comparison. This supports the idea that upon spreading the colloid onto the surface of water, fast evaporation of the volatile solvent leads to the formation of small, crystalline domains. Within these domains the interparticle spacing is determined by dodecanethiol concentration. Driven by surface tension, these crystalline domains form macroscopic islands which also contain significant voids. Further compression merely gathers these islands together and reduces the average interdomain correlation length, without affecting the interparticle separation within the domains. The pressure independence of the diffraction peaks agrees with our previous measurements of gold nanoparticle monolayers prepared using toluene as spreading solvents and without excess

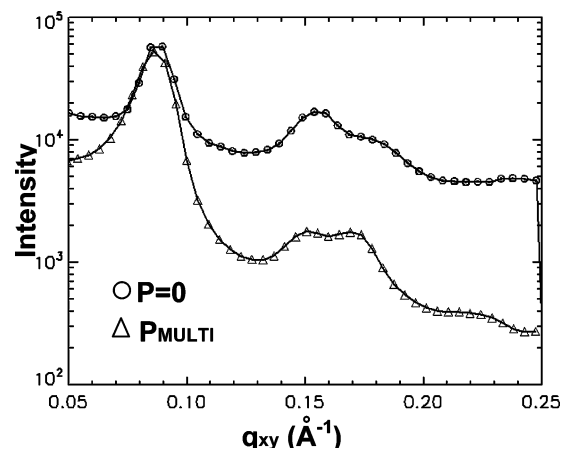


Figure 8. Diffraction peaks from partially thiolated T-Au as a function versus q_{xy} . The top profile (circles) is obtained at a surface pressure close to zero. The bottom profile (triangles) is obtained at P_{MONO} .

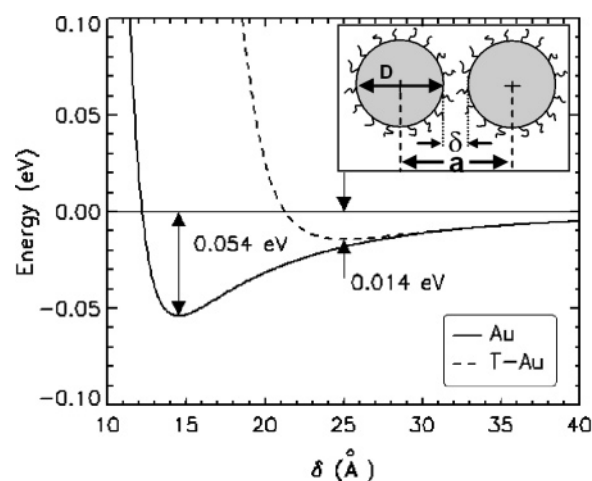


Figure 9. Calculated interparticle potential energy for gold nanoparticles as a function of interparticle spacing (δ). Well depth for each case is shown. See text for calculation details. Inset illustrates relative distances, where D = gold core diameter, a = center-to-center interparticle separation determined from GIXD, and $\delta = a - D$ equals the interparticle (edge-to-edge) spacing.

thiol.⁴⁸ Studies by others have also shown that Langmuir monolayers of gold particles form fairly rigid lattices in which lattice spacing remains unchanged as pressure is increased.^{43,44,49}

Subtraction of the average diameter of the gold cores ($D = 6.0 \text{ nm}$) from the center-to-center separation distances determined above results in interparticle (edge-to-edge) spacing values of $\delta = 1.4 \text{ nm}$ for Au and $\delta = 2.5 \text{ nm}$ for T-Au. The small δ value for the Au monolayer suggests that repeatedly washing the nanoparticles and redispersing them back into a clean heptane solvent can remove a significant portion of the dodecanethiol molecules that are originally ligated to the particle surface. This occurs because the unbound ligand molecules in the solvent are removed during the washing step, thus changing the equilibrium between the thiol ligated to the nanoparticles surface and the free thiol dissolved in the solvent.⁵⁰ In this low density surface coverage state, the thiol molecules easily deform and entangle, resulting in significant interdigitation between molecules from neighboring particles, and the interparticle spacing is thus smaller than the length of a single extended molecule ($\sim 1.77 \text{ nm}$). On the other hand, the addition of excess thiol in the T-Au samples leads to a more complete packing of thiol molecules on the surface of the nanoparticles. This results in much greater steric repulsion when the particles are com-

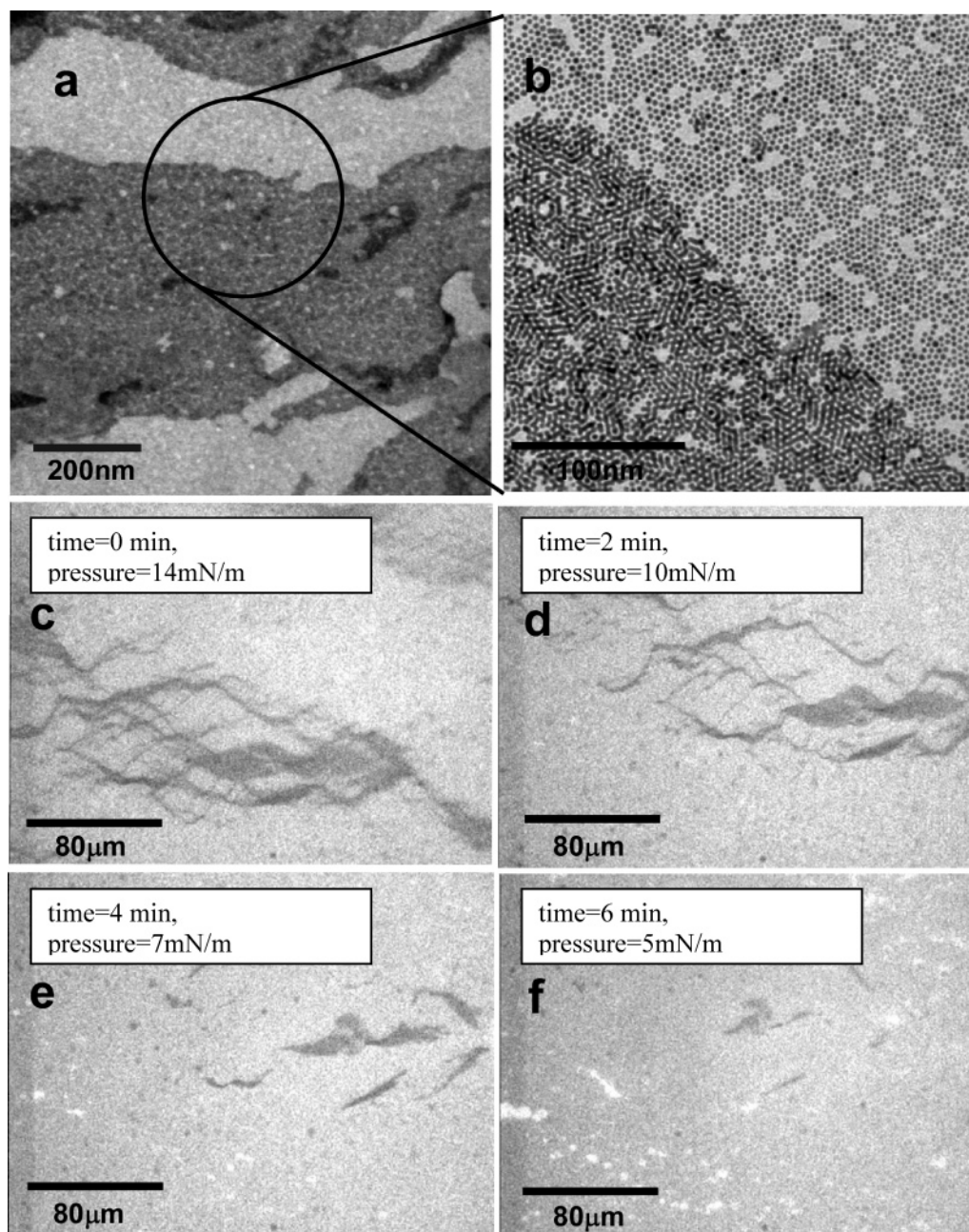


Figure 10. (a) TEM image of a wrinkled monolayer. (b) Zoomed-in view of the circled region in (a). (c–f) Optical microscopy images of four consecutive frames show the relaxation of a wrinkled T-Au monolayer during a continuous expansion of Langmuir trough barrier. Three shades are visible in these images (dark = wrinkles, gray = monolayer, white = water). The time between frames is about 2 min. Note that the direction of barrier motion is vertical in these images.

pressed, since the thiol molecules are forced to extend along the axial direction and have fewer conformational degrees of freedom. The interparticle gap spacing we measure for T-Au ($\delta = 2.5$ nm) is about 1.5 times the chain length of a thiol molecule, indicating only partial interdigitation of thiol molecules from neighboring particles. These results are consistent with analysis of the TEM micrograph of nanoparticle monolayer fabricated via colloidal droplet evaporation with or without excess thiol.⁵¹

It is instructive to consider the nature and magnitude of the interparticle interaction between a pair of nanoparticles for both Au and T-Au systems. It is well-known that van der Waals forces and steric repulsion are the main interactions between nanoparticles. Here, we adopt a model used by Ohara et al.³³ to estimate the attractive energy, V_{attract} as a function

of particle separation, δ , given as

$$V_{\text{attract}}(D) = -\frac{1.95 \text{ eV}}{12} \left\{ \frac{R}{\delta(1 + \delta/4R)} + \frac{1}{1 + \delta/R + \delta^2/4R^2} + 2 \ln \left[\frac{\delta(1 + \delta/4R)}{R(1 + \delta/R + \delta^2/4R^2)} \right] \right\}$$

where R is the radius of the particles. Figure 9 shows the calculated interparticle potential energy versus interparticle gap spacing for 6 nm gold spheres. The repulsive component of the potential (using $V_{\text{repulse}} = C(d_o/d)^{12}$) is adjusted for each case to yield energy minima at $\delta = 1.4$ nm (Au) and 2.5 nm (T-Au), corresponding to the interparticle spacings determined by GIXD. For Au samples, there is a relatively deeper potential

well of $\Delta E \sim 0.054$ eV compared to the potential well of $\Delta E \sim 0.014$ eV for T-Au.

The effect of a relatively shallow interaction potential for the T-Au system manifests itself very clearly when the highly compressed monolayers are expanded. Whereas wrinkles in the Au monolayer do not disperse, even over the course of a few days, the wrinkles formed in the T-Au monolayer disperse within minutes of expansion. Figure 10 shows the TEM micrographs of a T-Au multilayer area⁵² and its consecutive time-trace optical images upon expansion. These images show the complete dispersion of a wrinkled "island" within 10 min of breaking away from its neighbors. In fact, the T-Au film that had been entirely dispersed upon full expansion of the barrier can subsequently be recompressed to form a new monolayer. Cycled isotherms (not shown) for T-Au are entirely reversible, whereas the takeoff and roll-over features for Au shift to lower areas with each successive compression. The reversibility of the T-Au multilayer is associated with its shallow interparticle interaction potential well. Under the first-order approximation, the probability for the trilayer to unfold through a thermally activated process is proportional to $\exp(-2\Delta E/k_B T)$. The factor of 2 is associated with the interaction of a single particle in the middle layer with layers above and below. Thus for the T-Au system, the thermally activated unfolding probability (0.33) is much higher than that for the Au system (0.01). However, the above arguments are based upon a simple model calculation. Whether other factors, such as local ordering of the monolayer, contribute to the unfolding difference between Au and T-Au systems remains to be investigated.

The GIXD results also allow us to estimate the average size of the nanoparticle domains. These domains are crystalline arrangements of nanoparticles, not to be confused with the micrometer-to-millimeter size islands visible to the eye. Since GIXD is just a diffraction from a 2D grating, the relationship between diffraction peak width and grating/domain size follows the standard optical rule

$$\Delta\theta \approx \frac{\lambda}{L_D} \rightarrow k\Delta\theta = \Delta k \approx \frac{2\pi}{L_D}$$

where $\Delta\theta$ is the angular width of the peak, Δk is the inverse space width and L_D is the domain size. Using the $\{10\}$ diffraction peak, we measure widths of 0.015 and 0.012 \AA^{-1} for Au and T-Au, respectively. Inversion of these widths, using the rule above, yields approximate domain sizes (L_D) of 420 \AA (Au) and 520 \AA (T-Au). These are quite small, being on the order of 5–6 times the center-to-center particle spacings determined for each monolayer. Small domain sizes for Langmuir monolayers of gold nanoparticles were also observed by Fukuto et al.⁴⁹ In that work, the small domain size was attributed to polydispersity of particle sizes. In our case, the colloid is quite monodisperse, suggesting that small domain size is inherent to the Langmuir technique. The rapid evaporation of the spreading solvent and large initial surface area lead to the spontaneous formation of many small, ordered domains, tens of nanometers in diameter. These domains form macroscopic islands that also contain significant voids. Subsequent stages of compression initially bring these islands together (stage I compression) and later reduce the interstitial gaps between domains (stage II compression). However, the intrinsic glassy state caused by the jamming of many small ordered domains is difficult to be annealed out during the compression. It is also interesting to compare the different degrees of crystallinity in the monolayer formed through different techniques using the same nanoparticles, i.e., the LB technique and droplet

evaporation.^{24–26} Droplet evaporation uses a rapidly evaporating solvent such as toluene and can lead to ordered domains that extend to tens of micrometers. In that case, only a small number of domains initially form at the liquid–air interface. These domains grow continuously because there is a constant supply of nanoparticles to the liquid–air interface driven by evaporation.^{24–26}

IV. Conclusions

We have shown that Langmuir monolayers of highly monodisperse gold nanoparticles adopt a hexagonal packing symmetry where the interparticle spacing depends primarily upon thiol concentration. In contrast, surface pressure has little effect on this spacing. The correlation lengths of the monolayers are much smaller than those observed in films produced by droplet evaporation, due to the different mechanisms of self-assembly in each case. At high surface pressures, wrinkles consisting of multilayers of particles begin to form. The reversibility of wrinkled monolayers of gold nanoparticles in the samples with high thiol concentration is explained in terms of ligand-induced steric repulsion and its effect upon the magnitude of the van der Waals interparticle attraction. We propose that the thiol concentration can be used to tune the steric repulsion between the nanoparticles. We also note that the further understanding of the dynamics of monolayer wrinkling could offer important insights into the collapse and folding of biological membranes and cellular structures.^{53–55} Although these are very different systems, the underlying physics could be similar.

Acknowledgment. The authors thank KaYee Lee for helpful discussions and the use of an LB trough in her lab for some of the preliminary work. We also extend our thanks to undergraduate summer interns Teri Mosher, Krystyna Tate, and Jessica Murray for their help on preparing the monolayers. ChemMat-CARS Sector 15 is principally supported by the National Science Foundation and Department of Energy under Grant No. CHE0565344. This work is supported by the U.S. Department of Energy, Basic Energy Sciences, Office of Science, under Contract No. W-31-109-Eng-38.

Supporting Information Available: Detailed description of the simulation scheme to fit the X-ray reflectivity data. This material is available free of charge via the Internet at <http://pubs.acs.org>.

References and Notes

- (1) El-Sayed, M. A. *Acc. Chem. Res.* **2001**, *34*, 257.
- (2) Halperin, W. P. *Rev. Mod. Phys.* **1986**, *58*, 533.
- (3) Empedocles, S.; Bawendi, M. *Acc. Chem. Res.* **1999**, *32*, 389.
- (4) Skomski, R. *J. Phys.: Condens. Matter* **2003**, *15*, R841.
- (5) Collier, C. P.; Vossmeier, T.; Heath, J. R. *Annu. Rev. Phys. Chem.* **1998**, *49*, 371.
- (6) Pileni, M. P. *J. Phys. Chem. B* **2001**, *105*, 3358.
- (7) Murray, C. B.; Kagan, C. R.; Bawendi, M. G. *Science* **1995**, *270*, 1335.
- (8) Silly F.; Gusev, A. O.; Taleb, A. Charra, F.; Pileni, M.-P. *Phys. Rev. Lett.* **2000**, *84*, 5840.
- (9) Tran, T. B.; Beloborodov, I. S.; Lin, X. M.; Vinokur, V. M.; Jaeger, H. M. *Phys. Rev. Lett.* **2005**, *95*, 076806.
- (10) Parthasarathy, R.; Lin, X. M.; Elteto, K.; Rosenbaum, T. F.; Jaeger, H. M. *Phys. Rev. Lett.* **2004**, *92*, 076801.
- (11) Black, C. T.; Murray, C. B.; Sandstrom, R. L.; Sun, S. *Science* **2000**, *290*, 1131.
- (12) Daniel, M. -C.; Astruc, D. *Chem. Rev.* **2004**, *104*, 293.
- (13) *Optical Properties of Metal Clusters*; Kreibig, U., Vollmer, M., Eds.; Springer Series in Materials Science; Springer-Verlag: Berlin, 1995; Vol. 25.
- (14) Middleton A. A.; Wingreen, N. S. *Phys. Rev. Lett.* **1993**, *71*, 3198.

- (15) Rabani, E.; Reichman, D. R.; Geissler, P. L.; Brus, L. E. *Nature (London)* **2003**, 426, 271.
- (16) Stowell, C.; Korgel, B. A. *Nano. Lett.* **2001**, 1, 595.
- (17) Tang, J.; Ge, G. L.; Brus, L. E. *J. Phys. Chem. B* **2002**, 106, 5653.
- (18) Motte, L.; Billoudet, F.; Lacaze, E.; Douin, J.; Pileni, M. P. *J. Phys. Chem. B* **1997**, 101, 138.
- (19) Moriarty, P.; Taylor, M. D. R.; Brust, M. *Phys. Rev. Lett.* **2002**, 89, 248303.
- (20) Dutta J.; Hofmann, H. *Encycl. Nano. Nanotechnol.* **2003**, 10, 1.
- (21) Kim, F.; Kwan, S.; Akana, J.; Yang, P. *J. Am. Chem. Soc.* **2001**, 123, 4360.
- (22) Heath, J. R.; Knobler C. M.; Leff, D. V. *J. Phys. Chem. B* **1997**, 101, 189.
- (23) Fendler J. H.; Meldrum, F. C. *Adv. Mater. (Weinheim, Ger.)* **1995**, 7, 607.
- (24) Lin, X. M.; Jaeger, H. M.; Sorensen, C. M.; Klabunde, K. J. *J. Phys. Chem. B* **2001**, 105, 3353.
- (25) Narayanan, S.; Wang, J.; Lin, X. M. *Phys. Rev. Lett.* **2004**, 93, 135503.
- (26) Bigioni, T. P.; Lin, X. M.; Nguyen, T. T.; Corwin, E. I.; Witten, T. A.; Jaeger, H. M. *Nat. Mater.* **2006**, 5, 265.
- (27) Tao, A.; Kim F.; Hess, C.; Goldberger, J.; He, R.; Sun, Y.; Xia, Y.; Yang, P. *Nano. Lett.* **2003**, 3, 1229.
- (28) Paul, S.; Pearson, C.; Molloy, A.; Cousins, M. A.; Green, M.; Kolliopoulou, S.; Dimitrakis, P.; Normand, P.; Tsoukalas, D.; Petty, M. C. *Nano. Lett.* **2003**, 3, 533.
- (29) Brust, M.; Stuhr-Hansen, N.; Norgaard, K.; Christensen, J. B.; Nielsen, L. K.; Bjornhom, T. *Nano. Lett.* **2001**, 1, 189.
- (30) *Nanoparticles, Building Blocks for Nanotechnology*; Rotello, V., Ed.; Kluwer: New York, 2004.
- (31) Murray, C. B.; Kagen, C. R.; Bawendi, M. G. *Annu. Rev. Mater. Sci.* **2000**, 30, 545.
- (32) Gelbart, W. M.; Sear, R. P.; Heath J. R.; Chaney, S. *Faraday Discuss.* **1999**, 112, 299.
- (33) Ohara, P. C.; Leff, D. V.; Heath J. R.; Gelbart, W. M. *Phys. Rev. Lett.* **1995**, 75, 3466.
- (34) Kim, B.; Tripp, S. L.; Wei, A. *Mater. Res. Soc. Symp. Proc.* **2001**, 676, Y6.1.1.
- (35) Collier, C. P.; Saykally, R. J.; Shiang, J. J.; Henrichs, S. E.; Heath, J. R. *Science* **1997**, 277, 1978.
- (36) Ouyang, J.; Chu, C. W.; Szmanda, C. R.; Ma L.; Yang, Y. *Nat. Mater.* **2004**, 3, 918.
- (37) Jiang, C.; Markutsya, S.; Pikus, Y.; Tsukruk, V. V. *Nat. Mater.* **2004**, 3, 721.
- (38) Elghanian, R.; Storhoff, J. J.; Mucic, R. C.; Letsinger, R. L.; Mirkin, C. A. *Science* **1997**, 277, 1078.
- (39) Park, S. J.; Taton, T. A.; Mirkin, C. A. *Science* **2002**, 295, 1503.
- (40) Fukuto, M.; Penanen, K.; Heilmann, R. K.; Pershan, P. S. *J. Chem. Phys.* **1997**, 107, 5531.
- (41) Lin, X. M.; Sorensen, C. M.; Klabunde, K. J. *J. Nanopart. Res.* **2000**, 2, 157.
- (42) Lin, B.; Meron, M.; Gebhardt, J.; Graber, T.; Schlossman, M.; Viccaro, P. J. *Physica B (Amsterdam, Neth.)* **2003**, 336, 75.
- (43) Huang, S.; Minami, K.; Sakaue, H.; Shingubara, S.; Takahagi, T. *Langmuir* **2004**, 20, 2274.
- (44) Pei, L.; Mori, K.; Adachi, M. *Colloids Surf.* **2006**, 281, 44.
- (45) Owing to the relatively high atomic number of the particles, the scattering of X-rays from these monolayers is strong, although calculations suggest that the gold layer is not thick enough to shield the underlying water substrate. It is also important to note that particles "shadow" each other at all incident angles used in these measurements. This is supported by a simple geometric argument and justifies the comparison of experimentally determined electron density profiles to "smeared layer" box models.
- (46) Parratt, L. G. *Phys. Rev.* **1954**, 95 (2), 359.
- (47) This film was prepared with 0.4 times the initial concentration of dodecanethiol used in the T-Au spreading solution.
- (48) Unpublished data.
- (49) Fukuto, M.; Heilmann, R. K.; Pershan, P. S.; Badia A.; Lennox, R. B. *J. Chem. Phys.* **2004**, 120, 3446.
- (50) Schessler, H. M.; Karpovich, D. S.; Blanchard, G. J. *J. Am. Chem. Soc.* **1996**, 118, 9645.
- (51) Lin, X. M.; Parthasarathy, R.; Jaeger, H. M. In *Encyclopedia of Nanoscience and Nanotechnology*; Schwarz, J. A., Contescu, C., Putyera, K., Eds.; Marcel Dekker: New York, 2004; p 2245.
- (52) The TEM sample was prepared using a horizontal dipping method (or Langmuir-Schäfer technique) at P_{MULTI} pressure point. It is possible that the actual monolayer on the water interface is much more compact than what is shown in the TEM image. Some holes in the monolayer could be created through the relaxation of the film during the preparation of the TEM grid.
- (53) Diamant, H.; Witten, T. A.; Ege, C.; Gopal A.; Lee, K. Y. C. *Phys. Rev. E: Stat., Nonlinear, Soft Matter Phys.* **2001**, 63, 061602.
- (54) Diamant, H.; Witten, T. A.; Gopal A.; Lee, K. Y. C. *Europhys. Lett.* **2000**, 52, 171.
- (55) Chaieb, S.; Natrajan, V. K.; El-rahman, A. A. *Phys. Rev. Lett.* **2006**, 96, 078101.